The negatively charged nitrogen-vacancy centre in diamond: the electronic solution

The negatively charged nitrogen-vacancy centre in diamond: the electronic solution

M W Doherty[1,4]**, N B Manson**[2]**, P Delaney**[3] **and L C L Hollenberg**[1]

[1] School of Physics, University of Melbourne, Melbourne, Victoria 3010, Australia
[2] Laser Physics Centre, Research School of Physics and Engineering, Australian National University, Canberra, Australian Capital Territory 0200, Australia
[3] School of Mathematics and Physics, Queen's University Belfast, Belfast BT7 1NN, UK
E-mail: marcuswd@unimelb.edu.au

Abstract. The negatively charged nitrogen-vacancy centre is a unique defect in diamond that possesses properties highly suited to many applications, including quantum information processing, quantum metrology and biolabelling. Although the unique properties of the centre have been extensively documented and utilized, a detailed understanding of the physics of the centre has not yet been achieved. Indeed, there persist a number of points of contention regarding the electronic structure of the centre, such as the ordering of the dark intermediate singlet states. Without a detailed model of the centre's electronic structure, the understanding of the system's unique dynamical properties cannot effectively progress. In this work, the molecular model of the defect centre is fully developed to provide a self-consistent model of the complete electronic structure of the centre. The application of the model to describe the effects of electric, magnetic and strain interactions, as well as the variation of the centre's fine structure with temperature, provides an invaluable tool to those studying the centre and a means of designing future empirical and *ab initio* studies of this important defect.

[4] Author to whom any correspondence should be addressed.

Contents

1. Introduction

The negatively charged nitrogen-vacancy (NV$^-$) centre in diamond is a promising system for many quantum information processing [1], quantum metrology and biolabelling applications [2]. These applications include secure quantum key distribution [3], quantum computing [4], Q-switching in solid state photonic cavities [5], magnetometry [6], electric field sensing [7] and decoherence-based imaging [8]. There is significant interest in the centre primarily due to its well-documented capabilities of single-photon generation [9], long-lived coherence [10], spin coupling [11] and optical spin polarization and readout [12]. The observed properties of the centre include a strong optical zero phonon line (ZPL) at 1.945 eV [13], an infrared ZPL at 1.190 eV [14], a paramagnetic ground state triplet [15] and a strain [16], Zeeman [17] and Stark [18] affected excited state triplet. Recent experimental studies have also provided new information regarding the centre's excited state fine structure, its temperature dependence [19] and the presence of dynamic Jahn–Teller effects [20].

The NV$^-$ centre is a point defect of C_{3v} symmetry in diamond consisting of a substitutional nitrogen atom adjacent to a carbon vacancy (refer to figure 1). The observable properties of the centre are consistent with a six-electron model [21], where the electrons are postulated to consist of the five unpaired electrons of the nearest-neighbour nitrogen and carbon atoms to the vacancy and an additional electron trapped at the centre. The even number of electrons yields an integer spin system, and the use of spin resonance techniques [22] has confirmed that the electronic states are highly localized to the vacancy and its nearest neighbours and that the ground state is an $^3A_2$ triplet [15]. The high degree of localization supports the application of a molecular model of the electronic system of the centre, in which the centre's electronic states are described by configurations of molecular orbitals (MOs) initially constructed from linear combinations of the dangling sp^3 orbitals of the nearest-neighbour carbon and nitrogen atoms using group theoretical arguments.

Previous applications of the molecular model [21, 23, 24] have successfully described the zero field splitting of the ground triplet state due to spin–spin interaction, the ^3E excited triplet state and its fine structure induced by both spin–orbit and spin–spin interactions, and many aspects of the interactions of the triplet states with electric, magnetic and strain perturbations. However, being a semi-empirical model, unless the molecular model is fully developed in order to reduce the model's parameters to the minimal set, the model has limited ability to make definitive predictions on aspects of the electronic structure that cannot be directly observed and
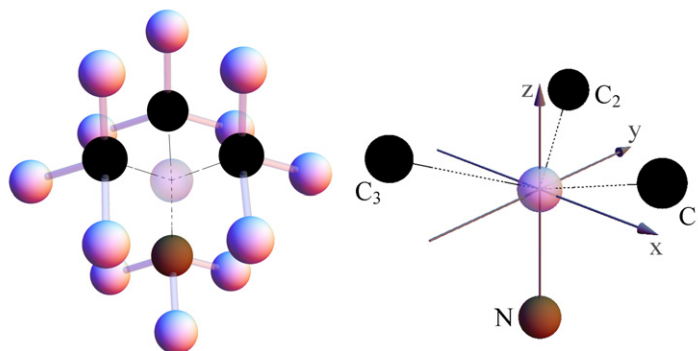
Figure 1. Schematics of the nitrogen-vacancy centre and lattice depicting the vacancy (transparent), the nearest-neighbour carbon atoms to the vacancy (black), the substitutional nitrogen atom (brown) and the next-to-nearest carbon neighbours to the vacancy (white). The adopted coordinate system and carbon labels are depicted in the right schematic.

the design of a systematic method to measure the large set of parameters becomes ambiguous. As a result of the previous partially developed molecular models, there have been a number of continual points of contention regarding the electronic structure of the centre. In particular, there is currently contention surrounding the energetic ordering and positioning of the dark ^1E and $^1A_1$ (and possibly $^1E'$) singlet states that are thought to exist between the ground and excited triplet states.

The locations of the intermediate singlet states are critical to developing an understanding of the process of optical spin polarization [12], which is the principal property of the NV^- centre that underpins the majority of its important applications. In the process of optical spin polarization, the population that has been optically excited from the ground to the excited triplet state is believed to decay non-radiatively from the excited triplet via the intermediate singlets to the ground triplet state in such a way that the $m_s = \pm 1$ sub-levels of the excited triplet state are preferentially depopulated and the $m_s = 0$ sub-level of the ground triplet is preferentially populated. Consequently, after a short period of optical excitation the centre becomes spin polarized into $m_s = 0$ population. This paper does not aim to describe the spin polarization mechanism, but instead provide the detailed model of the coupling of the intermediate singlet states and the triplet states due to spin–orbit interactions, which will form the foundation for future studies of the spin polarization mechanism.

There are a number of other properties of the NV^- centre that require a fully developed model in order to be satisfactorily explained. These include the Stark effect in the ground state triplet [7, 25], the small anisotropy of the effective electronic g-factor of the ground state triplet [26], the strain splitting of the infrared transition between the intermediate singlet states [14] and the presence of the Jahn–Teller effect in the ^1E and ^3E [20]. Each of these properties requires detailed treatment of electronic Coulomb repulsion, spin–orbit and spin–spin interactions that act to couple the electronic states of the centre and allow these properties to exist. The coupling of electronic states implies that the calculation of the effects of electric, magnetic and strain perturbations must be performed in the complete basis of the centre's electronic states.

In this paper, the molecular model of the NV^- centre will be fully developed to provide an electronic solution that is experimentally testable and offers explanations for many of the

remaining questions regarding the centre. The model will be based upon previous applications of the molecular model and utilize invaluable *ab initio* and empirical results to draw conclusions and identify parameters that are known. The electronic Coulomb, spin–orbit and spin–spin interactions will be treated to determine the energies and couplings of the electronic states. Spin–orbit and spin–spin interactions will be treated using perturbation theory in order to produce simple energy and coupling coefficient expressions in terms of the minimal set of model parameters. The parameters are provided as one- and two-electron matrix elements of the electronic interactions, allowing unambiguous evaluation by future *ab initio* studies. Electric, magnetic and strain interactions are also treated in order to allow future experiments to be designed for measuring the remaining unknown parameters. The treatment of the interactions will also provide the foundation to develop an understanding of spin polarization, the Jahn–Teller effect and the temperature dependence of the centre's properties.

2. The orbital structure

Adopting an adiabatic approximation and considering the nuclei of the crystal to be fixed at their equilibrium coordinates $\vec{R}_0$ corresponding to the ground electronic state, the electronic Hamiltonian of the NV^- centre can be defined as

$$\hat{H}_{NV} = \sum_i \hat{T}_i + \hat{V}_{Ne}(\vec{r}_i, \vec{R}_0) + \hat{V}_{so}(\mathbf{x}_i, \vec{R}_0) + \sum_{i>j} \hat{V}_{ee}(\mathbf{x}_i, \mathbf{x}_j) + \hat{V}_{ss}(\mathbf{x}_i, \mathbf{x}_j), \qquad (1)$$

where $\mathbf{x}_i = (\vec{r}_i, \vec{s}_i)$ denotes the collective spatial and spin coordinates of the ith electron of the centre, $\hat{T}_i$ is the kinetic energy of the ith electron, $\hat{V}_{Ne}$ is the effective Coulomb potential of the interaction of the nuclei and lattice electrons with the electrons of the centre, $\hat{V}_{so}$ is the electronic spin–orbit potential, $\hat{V}_{ee}$ is the Coulomb repulsion potential of the electrons of the centre and $\hat{V}_{ss}$ is the electronic spin–spin potential. Note that nuclear hyperfine interactions have been ignored. As for most molecular and solid state systems, the first step in solving $\hat{H}_{NV}$ is to obtain the solutions of the one-electron Coulomb problem,

$$\hat{h} = \hat{T} + \hat{V}_{Ne}(\vec{r}, \vec{R}_0), \qquad (2)$$

which will be the MOs of the centre. Using the MOs, a basis of many-electron configuration states that are solutions of $\sum_i \hat{h}_i$ can be defined and the remaining one- and two-electron components of $\hat{H}_{NV}$ can be treated in this basis.

At this stage, the C_{3V} symmetry of the ground nuclear equilibrium coordinates can be employed to construct the MOs of the defect. Using the basis $\{n, c_1, c_2, c_3\}$ (refer to figure 1 for labels) of tetrahedrally coordinated sp^3 atomic orbitals of the nearest-neighbour carbon and nitrogen atoms to the vacancy, the MOs can be constructed as linear combinations of the atomic orbitals (LCAOs) with definite orbital symmetry. This procedure has been conducted by a number of authors and an example of the resulting set of MOs [29] is

$$a_1(N) = n, \quad a_1(C) = \frac{1}{\sqrt{3}\sqrt{1 + 2S_{cc} - 3S_{nc}^2}}(c_1 + c_2 + c_3 - 3S_{nc}n),$$

$$e_x = \frac{1}{\sqrt{3}\sqrt{2 - 2S_{cc}}}(2c_1 - c_2 - c_3), \quad e_y = \frac{1}{\sqrt{2 - 2S_{cc}}}(c_2 - c_3), \qquad (3)$$

where $S_{nc} = \langle n|c_1 \rangle$ and $S_{cc} = \langle c_1|c_2 \rangle$ are orbital overlap integrals.
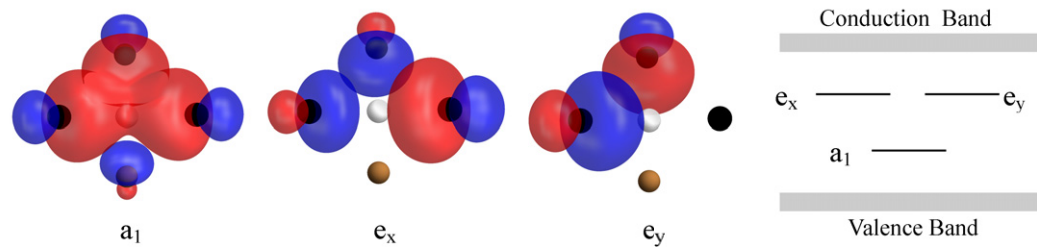
Figure 2. Schematics of the three NV centre MOs responsible for the centre's observable properties in the vicinity of the vacancy and their energy ordering. Red and blue components represent positive and negative contributions to the MOs, respectively, and the atom colours are the same as in figure 1.

Clearly, the LCAO method is a highly approximate method of constructing the MOs as it uses a restricted basis set and does not consider the interactions between the MOs of the defect centre and the electron orbitals of the remainder of the crystal. Therefore, the key objective of the LCAO method is not to produce an accurate description of the MOs, but to produce the correct number of MOs of a particular symmetry type and to estimate their energy ordering. The results of *ab initio* studies [27, 30, 31] can be used to confirm the number of MOs of each symmetry type and their energy ordering. The majority of *ab initio* studies agree that there exist three MOs $\{a_1, e_x, e_y\}$ within the bandgap of diamond and that these resemble the highly localized MOs of (3), with additional contributions from atomic orbitals at the next-to-nearest neighbours and beyond. Furthermore, the studies show that the $a_1(N)$ and $a_1(C)$ MOs have mixed to form a_1 and a_1' such that a_1' has been forced downwards in energy into the diamond valence band and a_1 has significant contributions from both the nitrogen and carbon atomic orbitals.

Using the six-electron model of the NV^- centre, the a_1' MO will be completely filled by two electrons in the ground $a_1'^2 a_1^2 e^2$ and first excited $a_1'^2 a_1^1 e^3$ MO configurations. There are several second excited MO configurations: $a_1'^2 e^4$, $a_1' a_1^2 e^3$ and $a_1' a_1 e^4$. Due to the estimated proximity of the a_1 MO to the valence band [29, 31], the first two second excited MO configurations $a_1'^2 e^4$ and $a_1' a_1^2 e^3$ could be close in energy. The states of these second excited MO configurations could mix with the states of the ground and first excited states and affect their energies, but are not expected to play a significant role in the centre's properties themselves. Consequently, only the three MOs within the bandgap are expected to contribute to the observable properties of the centre and only the ground and first excited MO configurations will be treated in detail in this work. Schematics of the three MOs in the region of the vacancy and their energy ordering are depicted in figure 2.

The configuration states of the ground and first excited MO configurations of the centre are constructed by first defining linear combinations of products of four MOs that transform as a particular row of an irreducible representation of the C_{3v} group. Using the irreducible representations and Clebsch–Gordan coefficients defined in [23], examples of the symmetrized linear combinations of products of two MOs are

$$\phi_{A_1}(a_1 a_1) = a_1 a_1, \quad \phi_{E,x}(a_1 e) = a_1 e_x, \quad \phi_{E,y}(a_1 e) = a_1 e_y,$$

$$\phi_{A_1}(ee) = \frac{1}{\sqrt{2}}(e_x e_x + e_y e_y), \quad \phi_{A_2}(ee) = \frac{1}{\sqrt{2}}(e_x e_y - e_y e_x), \tag{4}$$

$$\phi_{E,x}(ee) = \frac{1}{\sqrt{2}}(e_x e_x - e_y e_y), \quad \phi_{E,y}(ee) = \frac{-1}{\sqrt{2}}(e_x e_y + e_y e_x).$$

Table 1. The configuration and spin–orbit states of the NV^- centre expressed in terms of Slater determinants of the MOs. Second quantization notation has been adopted to denote the occupation of the MOs in each Slater determinant in the order $|a_1\bar{a}_1 e_x \bar{e}_x e_y \bar{e}_y\rangle$, where an overbar denotes spin-down.

		$\Phi^c_{j,k;S,m_s}$	$\Phi^{so}_{n,j,k}$
$a_1^2 e^2$	$^3A_2$	$\Phi^c_{A_2;1,0} = \frac{1}{\sqrt{2}}(|111001\rangle + |110110\rangle)$	$\Phi^{so}_{1,A_1} = \Phi^c_{A_2;1,0}$
		$\Phi^c_{A_2;1,1} = |111010\rangle$	$\Phi^{so}_{2,E,x} = \frac{-1}{\sqrt{2}}(-\Phi^c_{A_2;1,1} + \Phi^c_{A_2;1,-1})$
		$\Phi^c_{A_2;1,-1} = |110101\rangle$	$\Phi^{so}_{2,E,y} = \frac{-i}{\sqrt{2}}(\Phi^c_{A_2;1,1} + \Phi^c_{A_2;1,-1})$
	^1E	$\Phi^c_{E,x;0,0} = \frac{1}{\sqrt{2}}(|111100\rangle - |110011\rangle)$	$\Phi^{so}_{3,E,x} = \Phi^c_{E,x;0,0}$
		$\Phi^c_{E,y;0,0} = \frac{1}{\sqrt{2}}(|110110\rangle - |111001\rangle)$	$\Phi^{so}_{3,E,y} = \Phi^c_{E,y;0,0}$
	$^1A_1$	$\Phi^c_{A_1;0,0} = \frac{1}{\sqrt{2}}(|111100\rangle + |110011\rangle)$	$\Phi^{so}_{4,A_1} = \Phi^c_{A_1;0,0}$
$a_1 e^3$	^3E	$\Phi^c_{E,x;1,0} = \frac{1}{\sqrt{2}}(|100111\rangle + |011011\rangle)$	$\Phi^{so}_{5,E,x} = \frac{1}{2}[-i(\Phi^c_{E,x;1,1} + \Phi^c_{E,x;1,-1}) - (-\Phi^c_{E,y;1,1} + \Phi^c_{E,y;1,-1})]$
		$\Phi^c_{E,y;1,0} = \frac{1}{\sqrt{2}}(|101101\rangle + |011110\rangle)$	$\Phi^{so}_{5,E,y} = \frac{1}{2}[-(-\Phi^c_{E,x;1,1} + \Phi^c_{E,x;1,-1}) + i(\Phi^c_{E,y;1,1} + \Phi^c_{E,y;1,-1})]$
		$\Phi^c_{E,x;1,1} = |101011\rangle$	$\Phi^{so}_{6,E,x} = -\Phi^c_{E,y;1,0}$
		$\Phi^c_{E,y;1,1} = |101110\rangle$	$\Phi^{so}_{6,E,y} = \Phi^c_{E,x;1,0}$
		$\Phi^c_{E,x;1,-1} = |010111\rangle$	$\Phi^{so}_{7,A_2} = \frac{1}{2}[(-\Phi^c_{E,x;1,1} + \Phi^c_{E,x;1,-1}) + i(\Phi^c_{E,y;1,1} + \Phi^c_{E,y;1,-1})]$
		$\Phi^c_{E,y;1,-1} = |011101\rangle$	$\Phi^{so}_{8,A_1} = \frac{1}{2}[-i(\Phi^c_{E,x;1,1} + \Phi^c_{E,x;1,-1}) + (-\Phi^c_{E,y;1,1} + \Phi^c_{E,y;1,-1})]$
	$^1E'$	$\Phi^c_{E',x;0,0} = \frac{1}{\sqrt{2}}(|100111\rangle - |011011\rangle)$	$\Phi^{so}_{9,E,x} = \Phi^c_{E',x;0,0}$
		$\Phi^c_{E',y;0,0} = \frac{1}{\sqrt{2}}(|101101\rangle - |011110\rangle)$	$\Phi^{so}_{9,E,y} = \Phi^c_{E',y;0,0}$

The symmetrized combinations of products of four MOs can be constructed by repeating the process used to construct the above products of two MOs. Once the symmetrized products of occupied MOs corresponding to each configuration state are constructed, the configuration states are formed by performing a direct product with an associated spin state and transforming the result into a linear combination of Slater determinants. The resulting configuration states $\Phi^c_{j,k;S,m_s}$ have definite orbital symmetry (j denoting irreducible representation and k denoting row of the irreducible representation), total spin S and spin projection m_s, and are explicitly contained in table 1. Note that the construction of the configuration states in this way is completely analogous to LS coupling in atomic structure, where the atomic states are constructed to have definite orbital (L, m_l) and spin (S, m_s) quantum numbers prior to the introduction of spin–orbit interaction. The configuration states may also be expressed in terms of holes rather than electrons, and these expressions are contained in table A.1. However, the hole formalism will not be used in the remainder of this paper.

The configuration states are eigenstates of $\sum_i \hat{h}_i$, with each of the states of a MO configuration having the same eigenenergy as depicted on the left-hand side of figure 3. Employing the Wigner–Eckart theorem [32],

$$\langle \phi_{f,g} | \hat{O}_{p,q} | \phi_{j,k} \rangle = \begin{pmatrix} j & p & f \\ k & q & g \end{pmatrix}^* \langle \phi_f \| \hat{O}_p \| \phi_j \rangle, \tag{5}$$
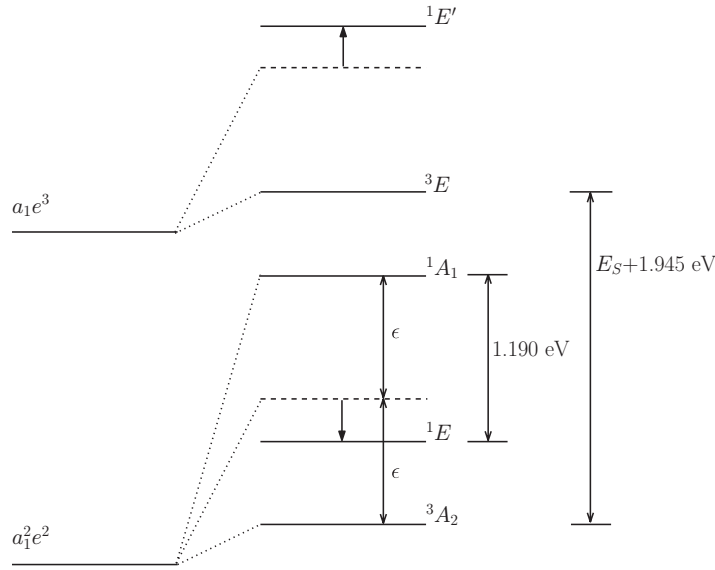
Figure 3. Energy level diagram of the orbital structure of the NV$^-$ centre. The MO configuration energies are depicted on the left-hand side, and the splitting into singlets and triplets due to the introduction of electronic Coulomb repulsion is depicted on the right-hand side. The dashed lines indicate the locations of the E singlet states prior to their Coulomb coupling. $\epsilon = 2\langle e_x e_x | \hat{V}_{ee} | e_y e_y \rangle$ is the difference in the Coulomb energies between the ground MO configuration states prior to the coupling of the E singlets. $E_S \approx 0.235$ eV is the Stokes shift of the optical ZPL.

where $\hat{O}$ is a tensor operator, (g, q, k) denote the rows of the irreducible representations (f, p, j) of the C_{3v} group, respectively, and $\langle \| \| \rangle$ is the reduced matrix element, the eigenenergies of each MO configuration can be expressed in terms of reduced matrix elements involving the MOs

$$a_1^2 e^2: \quad 2\langle a_1 \| \hat{h} \| a_1 \rangle + 2\langle e \| \hat{h} \| e \rangle, \quad a_1 e^3: \quad \langle a_1 \| \hat{h} \| a_1 \rangle + 3\langle e \| \hat{h} \| e \rangle. \tag{6}$$

The introduction of the Coulomb repulsion potential $\sum_{i>j} \hat{V}_{ee}(\mathbf{x}_i, \mathbf{x}_j)$ splits the MO configurations into distinct triplet and singlet energy levels. The diagonal matrix elements of the ground MO configuration triplet and singlets are

$$^3A_2: \quad C_0 + \langle \phi_{A_2}(ee) \| \hat{V}_{ee} \| \phi_{A_2}(ee) \rangle$$

$$^1E: \quad C_0 + \langle \phi_E(ee) \| \hat{V}_{ee} \| \phi_E(ee) \rangle$$

$$^1A_1: \quad C_0 + \langle \phi_{A_1}(ee) \| \hat{V}_{ee} \| \phi_{A_1}(ee) \rangle,$$

where

$$C_0 = \langle \phi_{A_1}(a_1 a_1) \| \hat{V}_{ee} \| \phi_{A_1}(ee) \rangle + 4\langle \phi_E(a_1 e) \| \hat{V}_{ee} \| \phi_E(a_1 e) \rangle - 2\langle \phi_E(a_1 e) \| \hat{V}_{ee} \| \phi_E(ea_1) \rangle.$$

Hund's rules indicate that the $^3A_2$ triplet is the ground electronic state, which implies that $\langle \phi_{A_2}(ee) \| \hat{V}_{ee} \| \phi_{A_2}(ee) \rangle < \langle \phi_E(ee) \| \hat{V}_{ee} \| \phi_E(ee) \rangle, \langle \phi_{A_1}(ee) \| \hat{V}_{ee} \| \phi_{A_1}(ee) \rangle$. The difference in the

singlet diagonal matrix elements is

$$\epsilon = \langle \phi_{A_1}(ee) \| \hat{V}_{ee} \| \phi_{A_1}(ee) \rangle - \langle \phi_E(ee) \| \hat{V}_{ee} \| \phi_E(ee) \rangle$$

$$= 2 \langle e_x e_x | \hat{V}_{ee} | e_y e_y \rangle$$

$$= 2 \int \rho_{xy}(\vec{r}_1) \hat{V}_{ee}(\vec{r}_1, \vec{r}_2) \rho_{xy}(\vec{r}_2) \, \mathrm{d}\vec{r}_1 \, \mathrm{d}\vec{r}_2, \tag{7}$$

where $\rho_{xy}(\vec{r}) = e_x(\vec{r}) e_y(\vec{r})$. The above integral is a standard exchange integral of a charge distribution $\rho(\vec{r})$, which has been proven to be positive definite. One such proof [33] from electrostatics uses Green's identity to show that

$$\int \rho(\vec{r}_1) \frac{1}{|\vec{r}_1 - \vec{r}_2|} \rho(\vec{r}_2) \, \mathrm{d}\vec{r}_1 \, \mathrm{d}\vec{r}_2 = \frac{1}{4\pi} \int |\vec{E}(\vec{r})|^2 \, \mathrm{d}\vec{r} \geqslant 0, \tag{8}$$

where $\vec{E}(\vec{r})$ is the electric field generated by the finite charge distribution $\rho(\vec{r})$. Thus, considering just the diagonal Coulomb matrix elements, the $^1A_1$ singlet must be higher in energy than the ^1E singlet. It has been shown that the difference in the diagonal Coulomb matrix elements of the ^1E singlet and $^3A_2$ triplet ($\langle \phi_E(ee) \| \hat{V}_{ee} \| \phi_E(ee) \rangle - \langle \phi_{A_2}(ee) \| \hat{V}_{ee} \| \phi_{A_2}(ee) \rangle$) is equal to the difference between the two singlets ϵ [34], thereby confirming the ordering indicated by Hund's rules and implying that the states of the ground configuration are equally spaced prior to coupling with states of higher MO configurations. Similar expressions for the diagonal Coulomb matrix elements were derived in [34]; however, without the proof that ϵ is positive definite, the ordering of the singlet and triplet states of the ground MO configuration was not conclusively demonstrated in [34]. In the first excited MO configuration, Hund's rules also indicate that the ^3E triplet has a smaller repulsion energy than the $^1E'$ singlet and a similar argument to that used for the singlet ordering in the ground MO configuration has been shown to confirm this ordering [35].

Since the only configuration states of the ground and first excited MO configurations that have both the same orbital symmetry and spin state are the ^1E and $^1E'$ singlets, these are the only states that are coupled by the Coulomb repulsion potential, and all of the other states are eigenstates of the orbital components of $\hat{H}_{NV}$, $\hat{H}_o = \sum_i \hat{h}_i + \sum_{i>j} \hat{V}_{ee}(\mathbf{x}_i, \mathbf{x}_j)$. The coupled E singlet states $\Phi^{c'}_{j,k;0,0}$ can be expressed as

$$\Phi^{c'}_{E,k;0,0} = N_\kappa \left[\Phi^c_{E,k;0,0} - \kappa \Phi^c_{E',k;0,0} \right],$$
$$\Phi^{c'}_{E',k;0,0} = N_\kappa \left[\Phi^c_{E',k;0,0} + \kappa \Phi^c_{E,k;0,0} \right], \tag{9}$$

where $k = x, y$ and the coupling coefficient κ is a function of the Coulomb repulsion matrix element $\langle \Phi^c_{E,k;0,0} | \hat{V}_{ee} | \Phi^c_{E',k;0,0} \rangle = \langle \phi_E(a_1 e) \| \hat{V}_{ee} \| \phi_E(ee) \rangle$,

$$\kappa = \frac{2 \langle \phi_E(a_1 e) \| \hat{V}_{ee} \| \phi_E(ee) \rangle}{E_{E';0} - E_{E;0} + \sqrt{(E_{E';0} - E_{E;0})^2 + 4 \langle \phi_E(a_1 e) \| \hat{V}_{ee} \| \phi_E(ee) \rangle^2}}, \tag{10}$$

and $N_\kappa = (1 + |\kappa|^2)^{-1/2}$ is the normalization constant. The interaction of the two E singlet states will also force the singlets apart in energy, shifting the lower ^1E singlet lower in energy towards the ground triplet state and shifting the higher $^1E'$ singlet further higher in energy than the excited triplet state.

Defining $E_{j;S}$ to be the orbital energies of the configuration states, the derived orbital structure prior to the introduction of spin–orbit and spin–spin interactions is depicted in figure 3. The known optical ZPL (1.945 eV) and infrared ZPL (1.190 eV) transition energies are also included in the figure. Notably, the energy separations of the triplet and singlet states have not yet been observed. As indicated by (6), there are different interactions between the electrons and nuclei in the ground and first excited MO configurations, such that (ignoring the Coulomb coupling of ^1E and $^1E'$) the configuration states of the ground MO configuration have the same nuclear equilibrium coordinates, and likewise the configuration states of the first excited MO configuration states have the same nuclear equilibrium coordinates, but these differ from the equilibrium coordinates of the ground MO configuration. Defining the energy of the ground $^3A_2$ state to be zero ($E_{A_2;1} = 0$), the energy of the $^1A_1$ singlet can be expressed as $E_{A_1;0} \approx E_{E;0} + 1.190$ eV, where the infrared ZPL has been directly used since, correct to first order in κ, both $^1A_1$ and ^1E have the same nuclear equilibrium coordinates. The energy of the excited ^3E triplet in the nuclear equilibrium coordinates of the ground MO configuration is $E_{E;1} = E_S + 1.945 \approx 2.180$ eV, where $E_S \approx 0.235$ eV is the Stokes shift of the optical transition [28]. Thus, the configuration energies $E_{E;0}$ and $E_{E';0}$ of the E singlet states, alongside their Coulomb coupling coefficient κ, are the first unknown parameters of the molecular model.

A recent *ab initio* study [31] concluded that the upper $^1E'$ singlet energetically crossed the ^3E triplet as the nearest-neighbour carbon and nitrogen nuclei were displaced while maintaining C_{3v} symmetry (nitrogen nucleus displaced inwards towards the vacancy and the carbon nuclei displaced outwards away from the vacancy). The preceding argument clearly shows that this can only be the case if there existed a strong Coulomb repulsion interaction between the $^1E'$ singlet and a higher energy E symmetric singlet. Such an interaction would force the $^1E'$ singlet lower in energy and if it were large enough, it could potentially overcome the repulsion from the lower ^1E singlet and the difference in the Coulomb energies between the $^1E'$ singlet and the ^3E triplet. The higher energy E singlet that produces this effect is most likely the $^1E''$ singlet that arises from the second excited MO configuration $a_1' a_1^2 e^3$. It is also possible that the higher energy E singlet arises from conduction band states. The other relevant second excited MO configuration $a_1'^2 e^4$ forms an $^1A_1'$ singlet. Consequently, the singlets of these two second excited MO configurations could potentially force the E and A_1 singlets of the ground and first excited MO configurations down in energy by different amounts, resulting in the $^1A_1$ crossing one of the E singlets. The most recent *ab initio* studies [30, 31] indicate that the ordering of the ground MO configuration singlets depicted in figure 3 is correct, and without further evidence that the second excited MO configuration states significantly shift the positions of the lower singlets, the simple orbital structure of figure 3 will be assumed. Due to the parametric formulation of the molecular model, the failure of this assumption will not affect the validity of the expressions derived in this analysis.

The recent *ab initio* study [30] indicates that the $^1A_1$ singlet is close to and possibly higher in energy than the ^3E triplet. As the quantitative values of the Coulomb repulsion matrix elements are not known, the preceding analysis cannot offer a definitive conclusion on the ordering of the $^1A_1$ singlet in relation to the ^3E triplet. The current understanding of the mechanisms of spin polarization and optical dynamics [24, 36] appears to strongly indicate that a singlet state is close, but lower in energy than the ^3E triplet. Therefore, further *ab initio* work is required to definitively determine the ordering of the $^1A_1$, ^3E and $^1E'$ states.

So far, it has been shown how the orbital structure of the NV$^-$ centre can be derived from the definition of the centre's MOs. The configuration states that have been obtained are solutions of the orbital components $\hat{H}_o$ of the centre's Hamiltonian and the orbital structure was determined up to the two unknown energies of the E symmetric singlets. The analysis of the Coulomb repulsion matrix elements has offered an insight into the contention surrounding the ordering of the intermediate singlet states. In the next section, the spin–orbit $\hat{V}_{so}$ and electronic spin–spin $\hat{V}_{ss}$ potentials will be treated as first-order perturbations to $\hat{H}_o$, and the fine structure and mixing of electronic spin of the centre will be determined.

3. The fine structure and mixing of electronic spin

The construction of the configuration states in the previous section to have a well-defined orbital symmetry aided in simplifying the treatment of the orbital components $\hat{H}_o$ of the centre's Hamiltonian. Since spin–orbit and spin–spin interactions act on both the electronic orbital and spin coordinates, their treatment can be likewise greatly simplified by constructing linear combinations of the configuration states that have well-defined spin–orbit symmetry. This can be done by first defining the combinations of the $S = 1, 0$ spin states ($|S, m_s\rangle$) that transform as particular rows of irreducible representations of the C_{3v} group [23]

$$S_{A_1} = |0, 0\rangle, \quad S_{A_2} = |1, 0\rangle,$$

$$S_{E,x} = \frac{-i}{\sqrt{2}}(|1, 1\rangle + |1, -1\rangle), \quad S_{E,y} = \frac{-1}{\sqrt{2}}(|1, 1\rangle - |1, -1\rangle). \tag{11}$$

In an analogous method to that used in constructing the combinations of products of two MOs that had well-defined symmetry, the above symmetrized spin states can be used in conjunction with the configuration states to construct the symmetrized spin–orbit states $\Phi^{so}_{n,j,k}$ contained in table 1, where n denotes the energy level and j and k denote the irreducible representation and row that the spin–orbit state transforms as in spin–orbit space.

The spin–orbit and spin–spin interaction potentials are [37]

$$\hat{V}_{so} = \frac{1}{2m^2c^2} \sum_i \vec{\nabla} \hat{V}_{Ne}(\vec{r}_i) \times \vec{p}_i \cdot \vec{s}_i \equiv \sum_i \vec{\lambda}_i \cdot \vec{\sigma}_i,$$

$$\hat{V}_{ss} = \frac{\mu_0 g_e^2 \mu_B^2}{4\pi\hbar^2} \sum_{i>j} \frac{\vec{s}_i \cdot \vec{s}_j}{|\vec{r}_{ij}|^3} - \frac{3(\vec{s}_i \cdot \vec{r}_{ij})(\vec{r}_{ij} \cdot \vec{s}_j)}{|\vec{r}_{ij}|^5} \equiv \sum_{i>j} \vec{\sigma}_i \cdot \bar{D}_{ij} \cdot \vec{\sigma}_j \tag{12}$$

where $\vec{p}_i$ and $\vec{s}_i = (\hbar/2)\vec{\sigma}_i$ are the momentum and spin operators of the ith electron, $\vec{r}_{ij} = \vec{r}_j - \vec{r}_i = x_{ij}\vec{x} + y_{ij}\vec{y} + z_{ij}\vec{z}$ ($\vec{x}, \vec{y}, \vec{z}$ are unit coordinate vectors), g_e is the free electron g-factor, and $\vec{\lambda}$ and $\bar{D}$ are rank one and two orbital tensor operators respectively. The components of the orbital tensor operators are

$$\vec{\lambda} = -\hat{\lambda}_{E,y}\vec{x} + \hat{\lambda}_{E,x}\vec{y} + \hat{\lambda}_{A_2}\vec{z},$$

$$\bar{D} = \begin{pmatrix} -\frac{1}{2}\hat{D}_{A_1} - \hat{D}_{E,x,1} & \hat{D}_{E,y,1} & -\hat{D}_{E,x,2} \\ \hat{D}_{E,y,1} & -\frac{1}{2}\hat{D}_{A_1} + \hat{D}_{E,x,1} & -\hat{D}_{E,y,2} \\ -\hat{D}_{E,x,2} & -\hat{D}_{E,y,2} & \hat{D}_{A_1} \end{pmatrix}, \tag{13}$$

Table 2. The matrix representation of the spin–orbit interaction potential in the basis $\{\Phi^{so}_{1,A_1}, \Phi^{so}_{2,E,x}, \Phi^{so}_{2,E,y}, \Phi^{so}_{3,E,x}, \Phi^{so}_{3,E,y}, \Phi^{so}_{4,A_1}, \Phi^{so}_{5,E,x}, \Phi^{so}_{5,E,y}, \Phi^{so}_{6,E,x}, \Phi^{so}_{6,E,y}, \Phi^{so}_{7,A_2}, \Phi^{so}_{8,A_1}, \Phi^{so}_{9,E,x}, \Phi^{so}_{9,E,y}\}$. The spin–orbit parameters $\lambda_\parallel$ and $\lambda_\perp$ are defined in table 4. The lower half of the matrix can be obtained using the Hermitian property of the spin–orbit potential.

$$
\begin{array}{cccccccccccccc}
0 & 0 & 0 & 0 & 0 & -2\mathrm{i}\lambda_\parallel & 0 & 0 & 0 & 0 & 0 & \sqrt{2}\lambda_\perp & 0 & 0 \\
  & 0 & 0 & 0 & 0 & 0 & 0 & -\lambda_\perp & 0 & 0 & 0 & 0 & -\mathrm{i}\lambda_\perp & 0 \\
  &   & 0 & 0 & 0 & 0 & -\lambda_\perp & 0 & 0 & 0 & 0 & 0 & 0 & -\mathrm{i}\lambda_\perp \\
  &   &   & 0 & 0 & 0 & -\mathrm{i}\sqrt{2}\lambda_\perp & 0 & 0 & 0 & 0 & 0 & 0 & 0 \\
  &   &   &   & 0 & 0 & 0 & -\mathrm{i}\sqrt{2}\lambda_\perp & 0 & 0 & 0 & 0 & 0 & 0 \\
  &   &   &   &   & 0 & 0 & 0 & 0 & 0 & 0 & \mathrm{i}\sqrt{2}\lambda_\perp & 0 & 0 \\
  &   &   &   &   &   & -\lambda_\parallel & 0 & 0 & 0 & 0 & 0 & 0 & 0 \\
  &   &   &   &   &   &   & -\lambda_\parallel & 0 & 0 & 0 & 0 & 0 & 0 \\
  &   &   &   &   &   &   &   & 0 & 0 & 0 & 0 & -\mathrm{i}\lambda_\parallel & 0 \\
  &   &   &   &   &   &   &   &   & 0 & 0 & 0 & 0 & -\mathrm{i}\lambda_\parallel \\
  &   &   &   &   &   &   &   &   &   & \lambda_\parallel & 0 & 0 & 0 \\
  &   &   &   &   &   &   &   &   &   &   & \lambda_\parallel & 0 & 0 \\
  &   &   &   &   &   &   &   &   &   &   &   & 0 & 0 \\
  &   &   &   &   &   &   &   &   &   &   &   &   & 0
\end{array}
$$

where

$$\hat{D}_{A_1} = \frac{\mu_0 g_e^2 \mu_{\mathrm{B}}^2}{16\pi |\vec{r}_{ij}|^3}\left(1 - \frac{3z_{ij}^2}{|\vec{r}_{ij}|^5}\right),$$

$$\hat{D}_{E,x,1} = \frac{\mu_0 g_e^2 \mu_{\mathrm{B}}^2}{32\pi |\vec{r}_{ij}|^3}\frac{3(x_{ij}^2 - y_{ij}^2)}{|\vec{r}_{ij}|^5}, \quad \hat{D}_{E,y,1} = -\frac{\mu_0 g_e^2 \mu_{\mathrm{B}}^2}{32\pi |\vec{r}_{ij}|^3}\frac{6x_{ij} y_{ij}}{|\vec{r}_{ij}|^5},$$

$$\hat{D}_{E,x,2} = \frac{\mu_0 g_e^2 \mu_{\mathrm{B}}^2}{16\pi |\vec{r}_{ij}|^3}\frac{3z_{ij} x_{ij}}{|\vec{r}_{ij}|^5}, \quad \hat{D}_{E,y,2} = \frac{\mu_0 g_e^2 \mu_{\mathrm{B}}^2}{16\pi |\vec{r}_{ij}|^3}\frac{3z_{ij} y_{ij}}{|\vec{r}_{ij}|^5}.$$

Using the spin–orbit states of table 1 and the above definitions of the tensor operators, the application of the Wigner–Eckart theorem allows the computation of the matrix representations of the spin–orbit and spin–spin potentials in terms of one- and two-electron reduced matrix elements. The matrix representations are contained in tables 2 and 3 and the reduced matrix element expressions are contained in table 4. Note that as only the spin–orbit states associated with the triplet configuration states have non-zero spin–spin matrix elements, the matrix representation of the spin–spin potential is presented in the reduced basis of triplet spin–orbit states. In order to maintain clarity, only the upper triangle of the matrix representations have been presented. The lower half can be inferred using the Hermitian property of the potentials and the fact that each of the reduced matrix element expressions is real.

In calculating the non-axial orbital components of the spin–orbit potential, it was concluded that the reduced matrix element $\langle e\|\lambda_E\|e\rangle$ must be zero and so it was not included in the matrix representation of table 2. This follows from the fact that as $\lambda_{E,x}$ is a purely imaginary Hermitian orbital operator and its diagonal matrix elements in the MO basis are $\langle e_x|\lambda_{E,x}|e_x\rangle = \frac{1}{\sqrt{2}}\langle e\|\lambda_E\|e\rangle = -\langle e_y|\lambda_{E,x}|e_y\rangle$, these diagonal matrix elements must vanish,

Table 3. The matrix representation of spin–spin interaction potential in the triplet basis $\{\Phi^{so}_{1,A_1}, \Phi^{so}_{2,E,x}, \Phi^{so}_{2,E,y}, \Phi^{so}_{5,E,x}, \Phi^{so}_{5,E,y}, \Phi^{so}_{6,E,x}, \Phi^{so}_{6,E,y}, \Phi^{so}_{7,A_2}, \Phi^{so}_{8,A_1}\}$. The spin–spin parameters are defined in table 4. The lower half of the matrix can be obtained using the Hermitian property of the spin–spin potential.

$-2D_{1,A_1}$	0	0	0	0	0	0	0	$\sqrt{2}D_{1,E,2}$
	D_{1,A_1}	0	$\sqrt{2}D_{1,E,1}$	0	$D_{1,E,2}$	0	0	0
		D_{1,A_1}	0	$\sqrt{2}D_{1,E,1}$	0	$D_{1,E,2}$	0	0
			D_{2,A_1}	0	$\sqrt{2}D_{2,E,2}$	0	0	0
				D_{2,A_1}	0	$\sqrt{2}D_{2,E,2}$	0	0
					$-2D_{2,A_1}$	0	0	0
						$-2D_{2,A_1}$	0	0
							$D_{2,A_1}-2D_{2,E,1}$	0
								$D_{2,A_1}+2D_{2,E,1}$

Table 4. The spin–orbit and spin–spin parameters of the molecular model expressed in terms of one- and two-electron reduced matrix elements containing the MOs. The reduced matrix elements can be related to the matrix elements of the spin–orbit and spin–spin operators (13) using the definition of the Wigner–Eckart theorem (5), the Clebsch–Gordan coefficients [23], the definitions of the two-electron orbitals (4) and the identifications $D_{E,x,1}, D_{E,y,1} \sim D_{E,1}$ and $D_{E,x,2}, D_{E,y,2} \sim D_{E,2}$. Known values [16] and estimated order of magnitude of unknown values are contained in the rightmost column.

Parameter	Expression	Value
$\lambda_\parallel$	$-i\langle e\|\lambda_{A_2}\|e\rangle$	5.3 GHz
$\lambda_\perp$	$\frac{-i}{\sqrt{2}}\langle a_1\|\lambda_E\|e\rangle$	$\sim$GHz
D_{1,A_1}	$2\langle \phi_{A_2}(ee)\|D_{A_1}\|\phi_{A_2}(ee)\rangle$	2.87/3 GHz
$D_{1,E,1}$	$4\langle \phi_E(ae)\|D_{E,1}\|\phi_{A_2}(ee)\rangle$	$\sim$MHz
$D_{1,E,2}$	$-4\langle \phi_E(ae)\|D_{E,2}\|\phi_{A_2}(ee)\rangle$	$\sim$MHz
D_{2,A_1}	$\langle \phi_E(ae)\|D_{A_1}\|\phi_E(ae)\rangle - \langle \phi_E(ae)\|D_{A_1}\|\phi_E(ea)\rangle$	1.42/3 GHz
$D_{2,E,1}$	$-2(\langle \phi_E(ae)\|D_{E,1}\|\phi_E(ae)\rangle - \langle \phi_E(ae)\|D_{E,1}\|\phi_E(ea)\rangle)$	1.55/2 GHz
$D_{2,E,2}$	$2(\langle \phi_E(ae)\|D_{E,2}\|\phi_E(ae)\rangle - \langle \phi_E(ae)\|D_{E,2}\|\phi_E(ea)\rangle)$	$200/\sqrt{2}$ MHz

implying that $\langle e\|\lambda_E\|e\rangle = 0$. In [34], this result $\langle e\|\lambda_E\|e\rangle = 0$ was stated without explicit analytical proof; however, Maze [34] did provide numerical evidence that supports this result. In a previous application of the molecular model to the fine structure of the excited triplet state [18], this conclusion was not made and the coupling of $\Phi^{so}_{5,E,k}$ and $\Phi^{so}_{6,E,k}$ was incorrectly assigned as arising from the non-axial spin–orbit interaction matrix element $-i\sqrt{2}\langle e\|\lambda_E\|e\rangle$ instead of the correct spin–spin interaction matrix element $\sqrt{2}D_{2,E,2}$ as contained in table 3. The observation that spin–spin interaction couples $\Phi^{so}_{5,E,k}$ and $\Phi^{so}_{6,E,k}$ has also been made independently in [34].

As the spin–orbit and spin–spin matrix elements are observed to be of the order of MHz–GHz [16, 18] and the energy separations of the singlet and triplet states are expected to be of the order of meV–eV ($\sim 10^2$–10^5 GHz), it is appropriate to treat the spin–orbit and spin–spin potentials together as first-order perturbations to $\hat{H}_o$. The configuration energies

Table 5. The electronic energies correct to first order in spin–orbit and spin–spin interactions. The energies calculated using the known parameters of table 4 are provided on the right column.

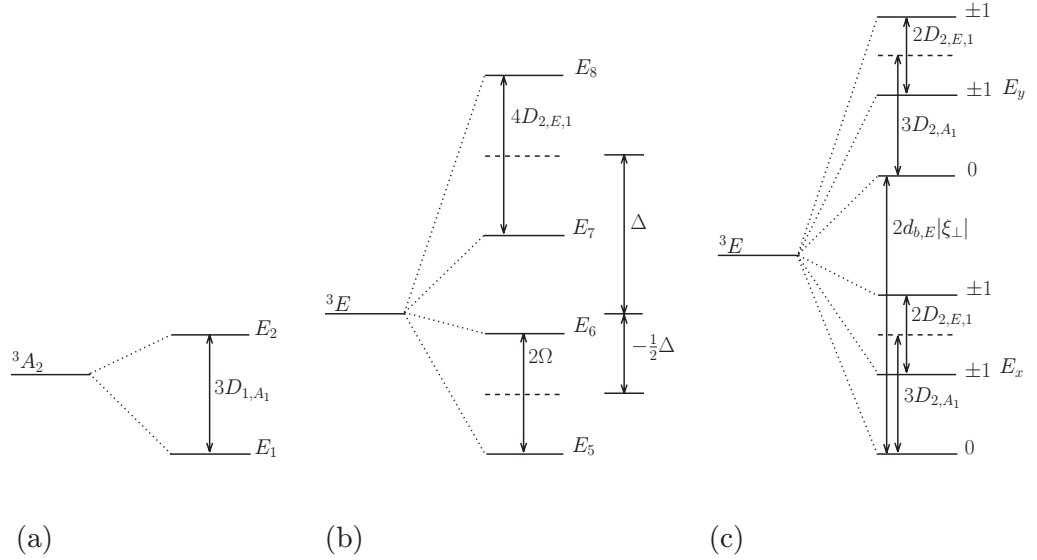| E_n $E_n^{(0)}$	$E_n^{(1)}$	Calculated
$E_1 = E_{A_2;1}$	$-2D_{1,A_1}$	$-1.91\,\mathrm{GHz}$
$E_2 = E_{A_2;1}$	$+D_{1,A_1}$	$0.957\,\mathrm{GHz}$
$E_3 = E_{E;0}$	$-$	$-$
$E_4 = E_{A_1;0}$	$-$	$-$
$E_5 = E_{E;1}$	$-\frac{1}{2}(\lambda_\parallel + D_{2,A_1}) - \frac{1}{2}[(\lambda_\parallel - 3D_{2,A_1})^2 + 8|D_{2,E,2}|^2]^{\frac{1}{2}}$	$E_{E;1} - 4.84\,\mathrm{GHz}$
$E_6 = E_{E;1}$	$-\frac{1}{2}(\lambda_\parallel + D_{2,A_1}) + \frac{1}{2}[(\lambda_\parallel - 3D_{2,A_1})^2 + 8|D_{2,E,2}|^2]^{\frac{1}{2}}$	$E_{E;1} - 0.936\,\mathrm{GHz}$
$E_7 = E_{E;1}$	$+\lambda_\parallel + D_{2,A_1} - 2D_{2,E,1}$	$E_{E;1} + 4.22\,\mathrm{GHz}$
$E_8 = E_{E;1}$	$+\lambda_\parallel + D_{2,A_1} + 2D_{2,E,1}$	$E_{E;1} + 7.32\,\mathrm{GHz}$
$E_9 = E_{E';0}$	$-$	$-$

(a)　　　　　　(b)　　　　　　(c)

Figure 4. Energy level diagrams of the fine structure of the $^3A_2$ and ^3E triplets of the NV$^-$ centre: (a) $^3A_2$ fine structure independent of strain; (b) ^3E fine structure in the absence of strain; and (c) ^3E fine structure in the limit of large non-axial strain $|\xi_\perp|$. Expressions for the energies E_n are contained in table 5 and $\Delta = \lambda_\parallel + D_{2,A_1}$ and $\Omega = \frac{1}{2}[(\lambda_\parallel - 3D_{2,A_1})^2 + 8|D_{2,E,2}|^2]^{1/2}$. The strain interaction parameter $d_{b,E}|\xi_\perp|$ is defined in (18).

$E_{j;S}$ and spin–orbit states $\{\Phi_{n,j,k}^{\mathrm{so}}\}$ are then the zero-order energies and electronic states of the perturbation expansion. The application of first-order perturbation theory yields the fine structure energies E_n contained in table 5 and depicted in figure 4 as well as the coupling coefficients contained in table A.2. The first-order corrected electronic states $\Phi_{n,j,k}^{\mathrm{so}'}$ are defined in terms of the coupling coefficients by

$$\Phi_{n,j,k}^{\mathrm{so}'} = N_n \left[s_{n,n}^{(0)} \Phi_{n,j,k}^{\mathrm{so}} + \sum_m (s_{n,m}^{(1)} + s_{n,m}^{(2)}) \Phi_{m,j,k}^{\mathrm{so}} \right], \tag{14}$$

where N_n is the normalization constant. The coefficient η contained in table A.2 is the coefficient that arises from the coupling of the degenerate $\Phi^{so}_{5,E,k}$ and $\Phi^{so}_{6,E,k}$ states of the ^{3}E triplet due to spin–spin interaction and is expressed in terms of the spin–orbit and spin–spin parameters as

$$\eta = \frac{2\sqrt{2}D_{2,E,2}}{\lambda_{\parallel} - 3D_{2,A_1} + [(\lambda_{\parallel} - 3D_{2,A_1})^2 + 8|D_{2,E,2}|^2]^{1/2}} \tag{15}$$

and $N_\eta = (1 + |\eta|^2)^{-1/2}$ is the associated normalization constant. Note that the coefficients $s^{(2)}_{n,m}$ do not denote coefficients that are truly second order in the spin–orbit and spin–spin parameters, but rather contain the first-order products of the Coulomb κ and degenerate spin–spin η coefficients with the other spin–orbit and spin–spin coefficients. As κ and η are expected to be orders of magnitude larger than the other spin–orbit and spin–spin coefficients, the $s^{(2)}_{n,m}$ coefficients may potentially be only slightly smaller than the $s^{(1)}_{n,m}$ coefficients.

The spin–orbit and spin–spin parameters that are contained in the first-order energies of table 5 have been determined in previous studies [16, 18] by directly observing the fine structure of the ground and excited triplet states and modelling the variation of the excited triplet fine structure with the application of strain and electric fields at low temperatures. The values of these known parameters are contained alongside the unknown parameters in table 4. The unknown parameters are all involved only in the first-order couplings of the spin–orbit states of the singlets and triplets and do not contribute to the first-order energies. Consequently, the effect of these unknown parameters can only be indirectly detected through the observation of interactions of the centre with electric, magnetic and strain perturbations that cannot be explained by the zero-order spin–orbit states and the coupling coefficients arising from the known parameters. Examples of such interactions are the presence of the Stark effect in the ground state triplet [7, 25] and the anisotropy of the ground state effective g-factor [26]. Frustratingly, it is precisely these unknown parameters that are likely to govern the process of spin polarization as they allow forbidden transitions between the triplet and singlet states; however, this will not be discussed further in this article. Using the known values of similar parameters, the estimated orders of magnitude of the unknown parameters are also contained in table 4.

4. Electric, magnetic and strain interactions

The Stark shift $\hat{V}_S$, Zeeman effect $\hat{V}_Z$ and strain $\hat{V}_\xi$ potentials that describe the centre's interaction with electric $\vec{E}$, magnetic $\vec{B}$ and effective strain $\vec{\xi}$ fields are

$$\hat{V}_S = \sum_i \vec{d}_i \cdot \vec{E}, \quad \hat{V}_Z = \frac{\mu_B}{\hbar} \sum_i (\vec{l}_i + g_e \vec{s}_i) \cdot \vec{B}, \quad \hat{V}_\xi = \sum_i \vec{d}_i \cdot \vec{\xi}, \tag{16}$$

where $\vec{d}_i = e\vec{r}_i$ is the electric dipole operator and $\vec{l}_i = \vec{r}_i \times \vec{p}_i$ is the orbital magnetic moment operator. Note that the above effective expression for the strain potential (in which strain is treated as an effective local electric field) is derived using the group operator replacement theorem [32] and can be unambiguously interpreted for uniaxial strain, but some care is required in its interpretation for non-uniaxial strain.

Each of these potentials contain operators that act on just the electronic orbital coordinates and can be written in terms of sums of orbital tensor operators with definite symmetry properties

$$\vec{d}_i = \hat{d}_{E,x}\vec{x} + \hat{d}_{E,y}\vec{y} + \hat{d}_{A_1}\vec{z}, \quad \vec{l}_i = -\hat{l}_{E,y}\vec{x} + \hat{l}_{E,x}\vec{y} + \hat{l}_{A_2}\vec{z}. \tag{17}$$
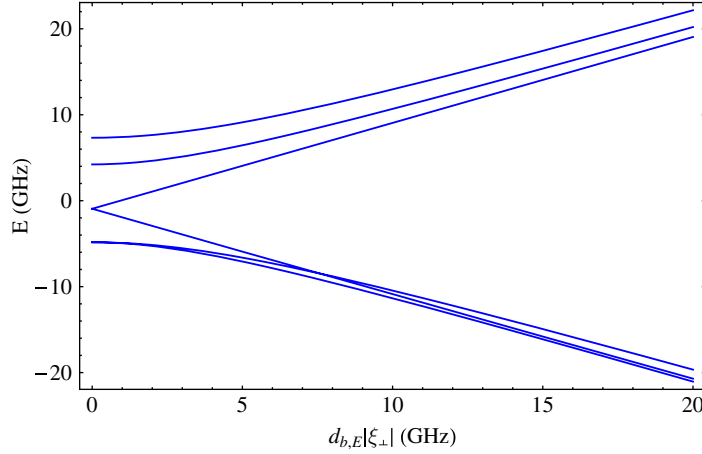
Figure 5. Plot of the variation of the ^{3}E triplet fine structure with the magnitude of the applied non-axial strain $|\xi_\perp|$. The plot was produced using the known spin–orbit and spin–spin parameters of table 4 and the matrix representation of the strain interaction (18).

As the spin–orbit states constructed in the last section are simple linear combinations of configuration states that have both well-defined orbital symmetry and spin, it is straightforward to apply the Wigner–Eckart theorem to calculate the matrix representations of each of the tensor orbital operators in terms of a set of reduced matrix elements. Since the expressions for the reduced matrix elements are identical for all orbital tensor operators of the same symmetry, the matrix representations of general orbital tensor operators $\hat{O} = \sum_i \hat{O}_i$ of each symmetry are contained in tables A.3 and A.4. The matrix representation of the electron spin operator $\vec{S} = \sum_i \vec{s}_i$ is contained in table A.5. These matrix representations can be immediately applied to calculate the effects of the different electric, magnetic and strain interactions in the basis of the zero-order spin–orbit states.

For example, the matrix representation of the strain potential in the basis of the zero-order spin–orbit states of the ^{3}E triplet $\{\Phi^{so}_{5,E,x}, \Phi^{so}_{5,E,y}, \Phi^{so}_{6,E,x}, \Phi^{so}_{6,E,y}, \Phi^{so}_{7,A_2}, \Phi^{so}_{8,A_1}\}$ is

$V_\xi[^3\mathrm{E}]$

$$
= \begin{pmatrix}
d_{b,A_1}\xi_z & 0 & 0 & 0 & -d_{b,E}\xi_y & -d_{b,E}\xi_x \\
0 & d_{b,A_1}\xi_z & 0 & 0 & d_{b,E}\xi_x & -d_{b,E}\xi_y \\
0 & 0 & d_{b,A_1}\xi_z + d_{b,E}\xi_x & -d_{b,E}\xi_y & 0 & 0 \\
0 & 0 & -d_{b,E}\xi_y & d_{b,A_1}\xi_z - d_{b,E}\xi_x & 0 & 0 \\
-d_{b,E}\xi_y & d_{b,E}\xi_x & 0 & 0 & d_{b,A_1}\xi_z & 0 \\
-d_{b,E}\xi_x & -d_{b,E}\xi_y & 0 & 0 & 0 & d_{b,A_1}\xi_z
\end{pmatrix}, \quad (18)
$$

where $d_{b,A_1} = \langle a_1\|d_{A_1}\|a_1\rangle + 3\langle e\|d_{A_1}\|e\rangle$ and $d_{b,E} = \langle e\|d_E\|e\rangle$. Previous studies [16, 18] have shown that the above matrix representation yields a strain variation of the ^{3}E triplet fine structure that agrees excellently with observation. A theoretical plot of the effect of non-axial strain is depicted in figure 5 and it clearly shows that non-axial strain splits the ^{3}E fine structure into upper and lower branches. Due to the $D_{2,E,2}$ spin–spin parameter that couples the $m_s = 0$ and

± 1 configuration states, there exist two level anti-crossings in the lower branch as the $m_s = 0$ changes from being the highest energy state of the lower branch to the lowest energy state [18]. In the vicinity of these anti-crossings, the states of the lower branch are all significant mixtures of the different spin sub-levels [18]. As there is no anti-crossing in the upper branch, the mixing of the spin sub-levels in the states of the upper branch does not significantly vary with strain [18].

In the limit of large strain the upper and lower branches become identical, with the same mixing and splitting of the spin sub-levels. This can be demonstrated by calculating the matrix representations of the spin–orbit, spin–spin and strain potentials in the basis of the ^{3}E configuration states $\{\Phi^c_{E,x;1,0}, \Phi^c_{E,x;1,1}, \Phi^c_{E,x;1,-1}, \Phi^c_{E,y;1,0}, \Phi^c_{E,y;1,1}, \Phi^c_{E,y;1,-1}\}$

$$V_{so}[^3E] + V_{ss}[^3E] = \left(\begin{array}{ccc|ccc} -2D_{2,A_1} & \frac{D_{2,E,2}}{\sqrt{2}} & -\frac{D_{2,E,2}}{\sqrt{2}} & 0 & \frac{-D_{2,E,2}}{\sqrt{2}} & \frac{-D_{2,E,2}}{\sqrt{2}} \\ \frac{D_{2,E,2}}{\sqrt{2}} & D_{2,A_1} & D_{2,E,1} & \frac{D_{2,E,2}}{\sqrt{2}} & \lambda_\| & -D_{2,E,1} \\ \frac{-D_{2,E,2}}{\sqrt{2}} & D_{2,E,1} & D_{2,A_1} & \frac{D_{2,E,2}}{\sqrt{2}} & D_{2,E,1} & -\lambda_\| \\ \hline 0 & \frac{D_{2,E,2}}{\sqrt{2}} & \frac{D_{2,E,2}}{\sqrt{2}} & -2D_{2,A_1} & \frac{-D_{2,E,2}}{\sqrt{2}} & \frac{D_{2,E,2}}{\sqrt{2}} \\ \frac{-D_{2,E,2}}{\sqrt{2}} & \lambda_\| & D_{2,E,1} & \frac{-D_{2,E,2}}{\sqrt{2}} & D_{2,A_1} & -D_{2,E,1} \\ \frac{-D_{2,E,2}}{\sqrt{2}} & -D_{2,E,1} & -\lambda_\| & \frac{D_{2,E,2}}{\sqrt{2}} & -D_{2,E,1} & D_{2,A_1} \end{array}\right), \tag{19}$$

$$V_\xi[^3E] = \left(\begin{array}{ccc|ccc} -d_{b,E}\xi_x & 0 & 0 & d_{b,E}\xi_y & 0 & 0 \\ 0 & -d_{b,E}\xi_x & 0 & 0 & d_{b,E}\xi_y & 0 \\ 0 & 0 & -d_{b,E}\xi_x & 0 & 0 & d_{b,E}\xi_y \\ \hline d_{b,E}\xi_y & 0 & 0 & d_{b,E}\xi_x & 0 & 0 \\ 0 & d_{b,E}\xi_y & 0 & 0 & d_{b,E}\xi_x & 0 \\ 0 & 0 & d_{b,E}\xi_y & 0 & 0 & d_{b,E}\xi_x \end{array}\right).$$

Clearly, if a ξ_x strain was applied such that $d_{b,E}\xi_x$ was much larger than the spin–orbit and spin–spin parameters, then the influence of the matrix elements of the upper right and lower left blocks would become insignificant and the configuration states would separate into identical E_x and E_y orbital branches. The off diagonal spin–spin matrix elements in the diagonal blocks are responsible for the mixing and splitting of the spin sub-levels within each branch. The fine structure of the ^{3}E triplet in the high strain limit is also depicted in figure 4.

Strain also affects the ^{1}E$'$ singlet and, only after the Coulomb coupling of the E singlets, affects the ^{1}E singlet as well at first order. The matrix representations of the strain potential correct to first order in κ in each of the corresponding basis sets $\{\Phi^{c'}_{3,E,x}, \Phi^{c'}_{3,E,y}\}$ and $\{\Phi^{c'}_{9,E,x}, \Phi^{c'}_{9,E,y}\}$ are

$$V_\xi[^1E] = N_\kappa^2 \begin{pmatrix} d_{a,A_1}\xi_z + 2\kappa d_{a,E}\xi_x & -2\kappa d_{a,E}\xi_y \\ -2\kappa d_{a,E}\xi_y & d_{a,A_1}\xi_z - 2\kappa d_{a,E}\xi_x \end{pmatrix},$$

$$V_\xi[^1E'] = N_\kappa^2 \begin{pmatrix} d_{b,A_1}\xi_z - (d_{b,E} + 2\kappa d_{a,E})\xi_x & (d_{b,E} + 2\kappa d_{a,E})\xi_y \\ (d_{b,E} + 2\kappa d_{a,E})\xi_y & d_{b,A_1}\xi_z + (d_{b,E} + 2\kappa d_{a,E})\xi_x \end{pmatrix}, \tag{20}$$

where $d_{a,A_1} = 2\langle a_1\|d_{A_1}\|a_1\rangle + 2\langle e\|d_{A_1}\|e\rangle$ and $d_{a,E} = \langle a_1\|d_E\|e\rangle$. The strain splitting of the $^1E'$ singlet has not yet been directly observed; however, the strain splitting of the ^1E singlet has been observed [14] in the strain dependence of the infrared transition at 1.190 eV, thereby confirming the coupling of the E symmetric singlets. Investigations of this strain splitting and the information that it can provide about the mixing of the E singlets are ongoing.

The matrix elements of tables A.3 and A.4 can be used to correlate the electric dipole moments of the centre. The electric dipole moments responsible for the optical transitions between the states of the ground and first excited MO configurations are all proportional to $d_{a,E}$. The electric dipole moment $d_{b,E}$ responsible for the observed Stark effect in ^3E is the same as the dipole moment of the infrared transition between $^1A_1$ and ^1E. Consequently, even though $^1A_1$ and ^1E belong to the same MO configuration, there is an appreciable dipole moment associated with the transition between them.

The operator matrix representations constructed in this section may also be used in conjunction with the first-order corrected spin–orbit states presented in the previous section to investigate the appearance of interactions at first and higher orders in the spin–orbit and spin–spin parameters. As discussed, these interactions provide important information on the unknown parameters and should be the subject of future investigations.

5. The room temperature electronic structure

The dynamic Jahn–Teller effect has been observed in the ^3E triplet [20]. This effect arises from the vibronic coupling of the spin–orbit states of the triplet [38]. The presence of the dynamic Jahn–Teller effect has the consequence that with increasing temperature E symmetric phonons drive transitions between the states of the triplet. The phonon rates are dependent on temperature and firstly are observed to give an unusual temperature dependence of the optical linewidths and at higher temperatures the phonon transition rates become much greater than the observable lifetimes of the states [39]. At this point, any population that is excited into one of the states is distributed to the other states that it is coupled with before any radiative decay can occur. If the phonon transitions distribute equal population to each of the coupled states, then the radiative transition will have the average energy of the coupled states. This process has been previously discussed in the literature as orbital averaging [19].

Since electron–phonon coupling is an orbital operator, the matrix representations (18) and (19) of an orbital operator in the ^3E triplet can be used to determine the selection rules of the phonon transitions. The allowed transitions are depicted in figure 6 for both the low and high strain cases. It is clear that for both the low and high strain cases, the phonon transitions will distribute population between the states of a particular spin projection, and since the transition matrix elements are identical for each transition, there will be approximately equal population distributed to each of the states of a given spin sub-level. Due to the coupling of the states with $m_s = \pm 1$ spin projections by the $D_{2,E,1}$ spin–spin parameter, the population will also be distributed between these sub-levels. Thus, regardless of strain, the fine structure of the ^3E triplet will average to a single splitting of $3D_{2,A_1} = 1.42$ GHz between the $m_s = 0$ and ± 1 spin sub-levels arising from spin–spin interaction (as depicted in figure 6). Therefore, as observed [19], the fine structure of the ^3E triplet at room temperature does not vary between NV$^-$ centres and appears as an effective orbital singlet split by spin–spin, similar to the ground $^3A_2$ triplet.
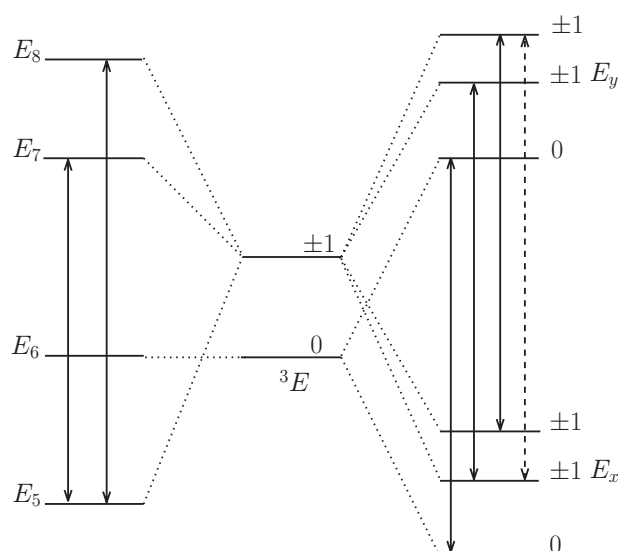
Figure 6. Schematics of the fine structure of the ^{3}E triplet at low temperature and low strain (left), at low temperature and high strain (right) and at ambient temperature (centre). The solid arrows indicate allowed phonon transitions and the dashed arrow indicates the transition allowed once $D_{2,E,1}$ spin–spin coupling within the two orbital branches in the high strain case is introduced. The plot demonstrates that if there were equal population in each of the phonon coupled states, the fine structure would average to the central structure with a single spin–spin splitting of $3D_{2,A_1} = 1.42$ GHz regardless of strain.

The matrix representations of orbital operators in the ^{1}E and ^{1}E′ singlets (20) indicate that these states should also be susceptible to the dynamic Jahn–Teller effect, although this has not yet been observed. The Jahn–Teller effect is likely to have significant consequences for the non-radiative dynamics of these states and influence their possible participation in the centre's spin polarization process. Clearly, the model of the Jahn–Teller effect in the NV$^-$ centre needs to be developed in greater detail to fully understand the temperature dependence of the centre's properties and the role of the Jahn–Teller effect in spin polarization.

6. Conclusion

In this paper, the molecular model of the NV$^-$ centre's electronic structure was developed in full. Through the explicit analysis of the Coulomb repulsion interaction, an insight was gained into the many competing factors that influence the energetic ordering of the singlet states of the ground and first excited MO configurations. Using a proof of the positive definite nature of the Coulomb repulsion separation of the states of the ground MO configuration, the simplest consistent orbital structure was adopted and the avenues of further investigation and routes to confirmation identified. Having obtained the orbital structure, spin–orbit and spin–spin interactions were treated using perturbation theory and the centre's fine structure and first-order state couplings were determined. The results were expressed in terms of the simplest set of one- and two-electron reduced matrix elements, allowing direct insight into which parameters

IOP Institute of Physics Φ DEUTSCHE PHYSIKALISCHE GESELLSCHAFT

were known and how to pursue the remaining unknown parameters. The calculation of the matrix representations of the centre's interactions with electric, magnetic and strain fields allowed an efficient discussion of the effects of strain on the centre's fine structure. The matrix representations also formed the basis of a short discussion of the temperature dependence of the centre's fine structure and highlighted the central role that the dynamic Jahn–Teller effect plays in the centre's dynamics.

Acknowledgments

Appendix

Table A.1. The configuration states expressed in terms of holes rather than electrons. Note that the hole formalism has not been used in this paper and these expressions are provided to assist the readers who have previously used the hole formalism.

		$\Phi^{\mathrm{c}}_{j,k;S,m_s}$	$\Phi^{\mathrm{so}}_{n,j,k}$
e^2	$^3A_2$	$\Phi^{\mathrm{c}}_{A_2;1,0} = \frac{1}{\sqrt{2}}(\lvert e_x\bar{e}_y\rangle + \lvert\bar{e}_x e_y\rangle)$	$\Phi^{\mathrm{so}}_{1,A_1} = \Phi^{\mathrm{c}}_{A_2;1,0}$
		$\Phi^{\mathrm{c}}_{A_2;1,1} = \lvert\bar{e}_x\bar{e}_y\rangle$	$\Phi^{\mathrm{so}}_{2,E,x} = \frac{-1}{\sqrt{2}}(-\Phi^{\mathrm{c}}_{A_2;1,1} + \Phi^{\mathrm{c}}_{A_2;1,-1})$
		$\Phi^{\mathrm{c}}_{A_2;1,-1} = \lvert e_x e_y\rangle$	$\Phi^{\mathrm{so}}_{2,E,y} = \frac{-i}{\sqrt{2}}(\Phi^{\mathrm{c}}_{A_2;1,1} + \Phi^{\mathrm{c}}_{A_2;1,-1})$
	^1E	$\Phi^{\mathrm{c}}_{E,x;0,0} = \frac{1}{\sqrt{2}}(\lvert e_y\bar{e}_y\rangle - \lvert e_x\bar{e}_x\rangle)$	$\Phi^{\mathrm{so}}_{3,E,x} = \Phi^{\mathrm{c}}_{E,x;0,0}$
		$\Phi^{\mathrm{c}}_{E,y;0,0} = \frac{1}{\sqrt{2}}(\lvert e_x\bar{e}_y\rangle - \lvert\bar{e}_x e_y\rangle)$	$\Phi^{\mathrm{so}}_{3,E,y} = \Phi^{\mathrm{c}}_{E,y;0,0}$
	$^1A_1$	$\Phi^{\mathrm{c}}_{A_1;0,0} = \frac{1}{\sqrt{2}}(\lvert e_y\bar{e}_y\rangle + \lvert e_x\bar{e}_x\rangle)$	$\Phi^{\mathrm{so}}_{4,A_1} = \Phi^{\mathrm{c}}_{A_1;0,0}$
$a_1 e$	^3E	$\Phi^{\mathrm{c}}_{E,x;1,0} = \frac{1}{\sqrt{2}}(\lvert\bar{a}_1 e_x\rangle + \lvert a_1\bar{e}_x\rangle)$	$\Phi^{\mathrm{so}}_{5,E,x} = \frac{1}{2}\left[-i(\Phi^{\mathrm{c}}_{E,x;1,1} + \Phi^{\mathrm{c}}_{E,x;1,-1})\right.$
			$\left.-(-\Phi^{\mathrm{c}}_{E,y;1,1} + \Phi^{\mathrm{c}}_{E,y;1,-1})\right]$
		$\Phi^{\mathrm{c}}_{E,y;1,0} = \frac{1}{\sqrt{2}}(\lvert\bar{a}_1 e_y\rangle + \lvert a_1\bar{e}_y\rangle)$	$\Phi^{\mathrm{so}}_{5,E,y} = \frac{1}{2}\left[-(-\Phi^{\mathrm{c}}_{E,x;1,1} + \Phi^{\mathrm{c}}_{E,x;1,-1})\right.$
			$\left.+i(\Phi^{\mathrm{c}}_{E,y;1,1} + \Phi^{\mathrm{c}}_{E,y;1,-1})\right]$
		$\Phi^{\mathrm{c}}_{E,x;1,1} = \lvert\bar{a}_1\bar{e}_x\rangle$	$\Phi^{\mathrm{so}}_{6,E,x} = -\Phi^{\mathrm{c}}_{E,y;1,0}$
		$\Phi^{\mathrm{c}}_{E,y;1,1} = \lvert\bar{a}_1\bar{e}_y\rangle$	$\Phi^{\mathrm{so}}_{6,E,y} = \Phi^{\mathrm{c}}_{E,x;1,0}$
		$\Phi^{\mathrm{c}}_{E,x;1,-1} = \lvert a_1 e_x\rangle$	$\Phi^{\mathrm{so}}_{7,A_2} = \frac{1}{2}\left[(-\Phi^{\mathrm{c}}_{E,x;1,1} + \Phi^{\mathrm{c}}_{E,x;1,-1})\right.$
			$\left.+i(\Phi^{\mathrm{c}}_{E,y;1,1} + \Phi^{\mathrm{c}}_{E,y;1,-1})\right]$
		$\Phi^{\mathrm{c}}_{E,y;1,-1} = \lvert a_1 e_y\rangle$	$\Phi^{\mathrm{so}}_{8,A_1} = \frac{1}{2}\left[-i(\Phi^{\mathrm{c}}_{E,x;1,1} + \Phi^{\mathrm{c}}_{E,x;1,-1})\right.$
			$\left.+(-\Phi^{\mathrm{c}}_{E,y;1,1} + \Phi^{\mathrm{c}}_{E,y;1,-1})\right]$
	$^1E'$	$\Phi^{\mathrm{c}}_{E',x;0,0} = \frac{1}{\sqrt{2}}(\lvert\bar{a}_1 e_x\rangle - \lvert a_1\bar{e}_x\rangle)$	$\Phi^{\mathrm{so}}_{9,E,x} = \Phi^{\mathrm{c}}_{E',x;0,0}$
		$\Phi^{\mathrm{c}}_{E',y;0,0} = \frac{1}{\sqrt{2}}(\lvert\bar{a}_1 e_y\rangle - \lvert a_1\bar{e}_y\rangle)$	$\Phi^{\mathrm{so}}_{9,E,y} = \Phi^{\mathrm{c}}_{E',y;0,0}$

Table A.2. The electronic coupling coefficients correct to first order in spin–orbit and spin–spin. Parameters are the same as defined in table 4.

$s_{n,m}$	$s_{n,m}^{(0)}$	$s_{n,m}^{(1)}$	$s_{n,m}^{(2)}$
$s_{1,1}=1$		–	–
$s_{1,4}=-$		$-2i\frac{\lambda_\parallel}{E_{A_1;0}}$	–
$s_{1,8}=-$		$-\sqrt{2}\frac{\lambda_\perp+D_{1,E,2}}{E_{E;1}}$	–
$s_{2,2}=1$		–	–
$s_{2,3}=-$		–	$iN_\kappa\kappa\frac{\lambda_\perp}{E_{E;0}}$
$s_{2,5}=-$		$-\sqrt{2}N_\eta\frac{D_{1,E,1}}{E_{E;1}}$	$-N_\eta\eta\frac{\lambda_\perp-D_{1,E,2}}{E_{E;1}}$
$s_{2,6}=-$		$N_\eta\frac{\lambda_\perp-D_{1,E,2}}{E_{E;1}}$	$-\sqrt{2}N_\eta\eta\frac{D_{1,E,1}}{E_{E;1}}$
$s_{2,9}=-$		$-iN_\kappa\frac{\lambda_\perp}{E_{E';0}}$	–
$s_{3,3}=N_\kappa$		–	–
$s_{3,2}=-$		–	$iN_\kappa\kappa\frac{\lambda_\perp}{E_{E;0}}$
$s_{3,5}=-$		$-i\sqrt{2}N_\kappa N_\eta\frac{\lambda_\perp}{E_{E;1}-E_{E;0}}$	–
$s_{3,6}=-$		–	$-iN_\kappa N_\eta\frac{\kappa\lambda_\parallel+\sqrt{2}\eta\lambda_\perp}{E_{E;1}-E_{E;0}}$
$s_{3,9}=-$		$-N_\kappa\kappa$	–
$s_{4,4}=1$		–	–
$s_{4,1}=-$		$-2i\frac{\lambda_\parallel}{E_{A_1;0}}$	–
$s_{4,8}=-$		$i\sqrt{2}\frac{\lambda_\perp}{E_{E;1}-E_{A_1;0}}$	–
$s_{5,5}=N_\eta$		–	–
$s_{5,2}=-$		$\sqrt{2}N_\eta\frac{D_{1,E,1}}{E_{E;1}}$	$N_\eta\eta\frac{\lambda_\perp-D_{1,E,2}}{E_{E;1}}$
$s_{5,3}=-$		$-i\sqrt{2}N_\kappa N_\eta\frac{\lambda_\perp}{E_{E;1}-E_{E;0}}$	–
$s_{5,6}=-$		$-N_\eta\eta$	–
$s_{5,9}=-$		–	$iN_\kappa N_\eta\frac{\eta\lambda_\parallel+\sqrt{2}\kappa\lambda_\perp}{E_{E';0}-E_{E;1}}$
$s_{6,6}=N_\eta$		–	–
$s_{6,2}=-$		$-N_\eta\frac{\lambda_\perp-D_{1,E,2}}{E_{E;1}}$	$\sqrt{2}N_\eta\eta\frac{D_{1,E,1}}{E_{E;1}}$
$s_{6,3}=-$		–	$-iN_\kappa N_\eta\frac{\kappa\lambda_\parallel+\sqrt{2}\eta\lambda_\perp}{E_{E;1}-E_{E;0}}$
$s_{6,5}=-$		$N_\eta\eta$	–
$s_{6,9}=-$		$-iN_\kappa N_\eta\frac{\lambda_\parallel}{E_{E';0}-E_{E;1}}$	–
$s_{7,7}=1$		–	–
$s_{8,8}=1$		–	–
$s_{8,1}=-$		$\sqrt{2}\frac{\lambda_\perp+D_{1,E,2}}{E_{E;1}}$	–
$s_{8,4}=-$		$i\sqrt{2}\frac{\lambda_\perp}{E_{E;1}-E_{A_1;0}}$	–
$s_{9,9}=N_\kappa$		–	–
$s_{9,2}=-$		$-iN_\kappa\frac{\lambda_\perp}{E_{E';0}}$	–
$s_{9,3}=-$		$N_\kappa\kappa$	–
$s_{9,5}=-$		–	$iN_\kappa N_\eta\frac{\eta\lambda_\parallel+\sqrt{2}\kappa\lambda_\perp}{E_{E';0}-E_{E;1}}$
$s_{9,6}=-$		$-iN_\kappa N_\eta\frac{\lambda_\parallel}{E_{E';0}-E_{E;1}}$	–

Table A.3. Combined matrix representation of $\hat{O}_{A_1}$ and $\hat{O}_{A_2}$ orbital operators in the basis $\{\Phi^{so}_{1,A_1}, \Phi^{so}_{2,E,x}, \Phi^{so}_{2,E,y}, \Phi^{so}_{3,E,x}, \Phi^{so}_{3,E,y}, \Phi^{so}_{4,A_1}, \Phi^{so}_{5,E,x}, \Phi^{so}_{5,E,y},$ $\Phi^{so}_{6,E,x}, \Phi^{so}_{6,E,y}, \Phi^{so}_{7,A_2}, \Phi^{so}_{8,A_1}, \Phi^{so}_{9,E,x}, \Phi^{so}_{9,E,y}\}$. To obtain the matrix representation of $\hat{O}_{A_1}$, set $O_{A_2} \to 0$, $O_{a,A_1} \to 2(\langle a_1\|V_{A_1}\|a_1\rangle + \langle e\|V_{A_1}\|e\rangle)$ and $O_{b,A_1} \to \langle a_1\|V_{A_1}\|a_1\rangle + 3\langle e\|V_{A_1}\|e\rangle$. To obtain the matrix representation of $\hat{O}_{A_2}$, set $O_{A_2} \to \langle e\|V_{A_2}\|e\rangle$, $O_{a,A_1} \to 0$ and $O_{b,A_1} \to 0$.

O_{a,A_1}	0	0	0	0	0	0	0	0	0	0	0	0	0
0	O_{a,A_1}	0	0	0	0	0	0	0	0	0	0	0	0
0	0	O_{a,A_1}	0	0	0	0	0	0	0	0	0	0	0
0	0	0	O_{a,A_1}	$2O_{A_2}$	0	0	0	0	0	0	0	0	0
0	0	0	$-2O_{A_2}$	O_{a,A_1}	0	0	0	0	0	0	0	0	0
0	0	0	0	0	O_{a,A_1}	0	0	0	0	0	0	0	0
0	0	0	0	0	0	O_{b,A_1}	O_{A_2}	0	0	0	0	0	0
0	0	0	0	0	0	$-O_{A_2}$	O_{b,A_1}	0	0	0	0	0	0
0	0	0	0	0	0	0	0	O_{b,A_1}	$-O_{A_2}$	0	0	0	0
0	0	0	0	0	0	0	0	O_{A_2}	O_{b,A_1}	0	0	0	0
0	0	0	0	0	0	0	0	0	0	O_{b,A_1}	$-O_{A_2}$	0	0
0	0	0	0	0	0	0	0	0	0	O_{A_2}	O_{b,A_1}	0	0
0	0	0	0	0	0	0	0	0	0	0	0	O_{b,A_1}	$-O_{A_2}$
0	0	0	0	0	0	0	0	0	0	0	0	O_{A_2}	O_{b,A_1}

Table A.4. Combined matrix representation of $\hat{O}_{E,x}$ and $\hat{O}_{E,y}$ orbital operators in the basis $\{\Phi^{so}_{1,A_1}, \Phi^{so}_{2,E,x}, \Phi^{so}_{2,E,y}, \Phi^{so}_{3,E,x}, \Phi^{so}_{3,E,y}, \Phi^{so}_{4,A_1}, \Phi^{so}_{5,E,x}, \Phi^{so}_{5,E,y},$ $\Phi^{so}_{6,E,x}, \Phi^{so}_{6,E,y}, \Phi^{so}_{7,A_2}, \Phi^{so}_{8,A_1}, \Phi^{so}_{9,E,x}, \Phi^{so}_{9,E,y}\}$. To obtain the matrix representation of $\hat{O}_{E,x}$, set $O_{a,x} \to \frac{1}{\sqrt{2}}\langle a_1\|V_E\|e\rangle$, $O_{a,y} \to 0$, $O_{b,x} \to \frac{1}{\sqrt{2}}\langle e\|V_E\|e\rangle$ and $O_{b,y} \to 0$. To obtain the matrix representation of $\hat{O}_{E,y}$, set $O_{a,y} \to \frac{1}{\sqrt{2}}\langle a_1\|V_E\|e\rangle$, $O_{a,x} \to 0$, $O_{b,y} \to \frac{1}{\sqrt{2}}\langle e\|V_E\|e\rangle$ and $O_{b,x} \to 0$.

0	0	0	0	0	0	0	0	$O_{a,x}$	$O_{a,y}$	0	0	0	0
0	0	0	0	0	0	$-\frac{O_{a,x}}{\sqrt{2}}$	$\frac{O_{a,y}}{\sqrt{2}}$	0	0	$-\frac{O_{a,y}}{\sqrt{2}}$	$\frac{O_{a,x}}{\sqrt{2}}$	0	0
0	0	0	0	0	0	$\frac{O_{a,y}}{\sqrt{2}}$	$\frac{O_{a,x}}{\sqrt{2}}$	0	0	$\frac{O_{a,x}}{\sqrt{2}}$	$\frac{O_{a,y}}{\sqrt{2}}$	0	0
0	0	0	0	0	$2O_{b,x}$	0	0	0	0	0	0	$-O_{a,x}$	$O_{a,y}$
0	0	0	0	0	$2O_{b,y}$	0	0	0	0	0	0	$O_{a,y}$	$O_{a,x}$
0	0	0	$2O_{b,x}$	$2O_{b,y}$	0	0	0	0	0	0	0	$O_{a,x}$	$O_{a,y}$
0	$-\frac{O^*_{a,x}}{\sqrt{2}}$	$\frac{O^*_{a,y}}{\sqrt{2}}$	0	0	0	0	0	0	0	$-O_{b,y}$	$-O_{b,x}$	0	0
0	$\frac{O^*_{a,y}}{\sqrt{2}}$	$\frac{O^*_{a,x}}{\sqrt{2}}$	0	0	0	0	0	0	0	$O_{b,x}$	$-O_{b,y}$	0	0
$O^*_{a,x}$	0	0	0	0	0	0	0	$O_{b,x}$	$-O_{b,y}$	0	0	0	0
$O^*_{a,y}$	0	0	0	0	0	0	0	$-O_{b,y}$	$-O_{b,x}$	0	0	0	0
0	$-\frac{O^*_{a,y}}{\sqrt{2}}$	$\frac{O^*_{a,x}}{\sqrt{2}}$	0	0	0	$-O_{b,y}$	$O_{b,x}$	0	0	0	0	0	0
0	$\frac{O^*_{a,x}}{\sqrt{2}}$	$\frac{O^*_{a,y}}{\sqrt{2}}$	0	0	0	$-O_{b,x}$	$-O_{b,y}$	0	0	0	0	0	0
0	0	0	$-O^*_{a,x}$	$O^*_{a,y}$	$O^*_{a,x}$	0	0	0	0	0	0	$-O_{b,x}$	$O_{b,y}$
0	0	0	$O^*_{a,y}$	$O^*_{a,x}$	$O^*_{a,y}$	0	0	0	0	0	0	$O_{b,y}$	$O_{b,x}$

Table A.5. Combined matrix representation of the components of the total spin operator $\vec{S}$ in the basis $\{\Phi^{so}_{1,A_1}, \Phi^{so}_{2,E,x}, \Phi^{so}_{2,E,y}, \Phi^{so}_{3,E,x}, \Phi^{so}_{3,E,y}, \Phi^{so}_{4,A_1}, \Phi^{so}_{5,E,x}, \Phi^{so}_{5,E,y}, \Phi^{so}_{6,E,x}, \Phi^{so}_{6,E,y}, \Phi^{so}_{7,A_2}, \Phi^{so}_{8,A_1}, \Phi^{so}_{9,E,x}, \Phi^{so}_{9,E,y}\}$. To obtain the matrix representation of $\hat{S}_x$, set $S_x \to \hbar$ and $S_y, S_z \to 0$. To obtain the matrix representation of $\hat{S}_y$, set $S_y \to \hbar$ and $S_x, S_z \to 0$. To obtain the matrix representation of $\hat{S}_z$, set $S_z \to \hbar$ and $S_x, S_y \to 0$.

0	iS_y	$-iS_x$	0	0	0	0	0	0	0	0	0	0	0
$-iS_y$	0	$-iS_z$	0	0	0	0	0	0	0	0	0	0	0
iS_x	iS_z	0	0	0	0	0	0	0	0	0	0	0	0
0	0	0	0	0	0	0	0	0	0	0	0	0	0
0	0	0	0	0	0	0	0	0	0	0	0	0	0
0	0	0	0	0	0	0	0	0	0	0	0	0	0
0	0	0	0	0	0	0	iS_z	$\frac{i}{\sqrt{2}}S_y$	$\frac{i}{\sqrt{2}}S_x$	0	0	0	0
0	0	0	0	0	0	$-iS_z$	0	$\frac{i}{\sqrt{2}}S_x$	$\frac{i}{\sqrt{2}}S_y$	0	0	0	0
0	0	0	0	0	0	$\frac{-i}{\sqrt{2}}S_y$	$\frac{-i}{\sqrt{2}}S_x$	0	0	$\frac{-i}{\sqrt{2}}S_x$	$\frac{i}{\sqrt{2}}S_y$	0	0
0	0	0	0	0	0	$\frac{-i}{\sqrt{2}}S_x$	$\frac{-i}{\sqrt{2}}S_y$	0	0	$\frac{-i}{\sqrt{2}}S_y$	$\frac{-i}{\sqrt{2}}S_x$	0	0
0	0	0	0	0	0	0	0	$\frac{i}{\sqrt{2}}S_x$	$\frac{i}{\sqrt{2}}S_y$	0	iS_z	0	0
0	0	0	0	0	0	0	0	$\frac{-i}{\sqrt{2}}S_y$	$\frac{i}{\sqrt{2}}S_x$	$-iS_z$	0	0	0
0	0	0	0	0	0	0	0	0	0	0	0	0	0
0	0	0	0	0	0	0	0	0	0	0	0	0	0

References

[1] Wrachtrup J and Jelezko F 2006 *J. Phys.: Condens. Matter* **18** S807

[2] Fu C-C, Lee H-Y, Chen K, Lim T-S, Wu H-Y, Lin P-K, Wei P-K, Tsoa P-H, Chang H C and Fann W 2007 *Proc. Natl Acad. Sci. USA* **104** 727

Chang Y-R *et al* 2008 *Nat. Nanotech.* **3** 284

Neugart F, Zappe A, Jelezko F, Tietz C, Boudou J P, Krueger A and Wrachtrup J 2007 *Nano Lett.* **7** 3588

Cuche A, Sonnefraud Y, Faklaris O, Garrot D, Boudou J P, Sauvage T, Roch J F, Treussart F and Huant S 2009 *J. Lumin.* **129** 1475

[3] Beveratos A, Brouri R, Gacoin T, Villing A, Poizat J P and Grangier P 2002 *Phys. Rev. Lett.* **89** 187901

[4] Jelezko F, Gaebel T, Popa I, Domhan M, Gruber A and Wrachtrup J 2004 *Phys. Rev. Lett.* **93** 130501

Gurudev Dutt M V, Childress L, Jiang L, Togan E, Maze J, Jelezko F, Zibrov A S, Hemmer P R and Lukin M D 2007 *Science* **316** 1312

Ladd T D, Jelezko F, Laflamme R, Nakamura Y, Monroe C and O'Brien J L 2010 *Nature* **464** 45

[5] Greentree A D, Salzman J, Prawer S and Hollenberg L C L 2006 *Phys. Rev.* A **73** 013818

[6] Balasubramanian G *et al* 2008 *Nature* **455** 648

Maze J R *et al* 2008 *Nature* **455** 644

Degen C L 2008 *Appl. Phys. Lett.* **92** 243111

Steinert S, Dolde F, Neumann P, Aird A, Naydenov B, Balasubramanian G, Jelezko F and Wrachtrup J 2010 *Rev. Sci. Instrum.* **81** 043705

Balasubramanian G *et al* 2009 *Nat. Mater.* **8** 383

Taylor J M, Cappellaro P, Childress L, Jiang L, Budker D, Hemmer P R, Yacoby A, Walsworth R and Lukin M D 2008 *Nat. Phys.* **4** 810

[7] Dolde F, Fedder H, Doherty M W, Nöbauer T, Rempp F, Balasubramanian G, Wolf T, Reinhard F, Hollenberg L C L, Jelezko F and Wrachtrup J 2011 in preparation

[8] Cole J H and Hollenberg L C L 2009 *Nanotechnology* **20** 495401
Hall L T, Cole J H, Hall C D and Hollenberg L C L 2009 *Phys. Rev. Lett.* **103** 220802
Hall L T, Hill C D, Cole J H and Hollenberg L C L 2010 *Phys. Rev.* B **82** 045208
Hall L T, Hill C D, Cole J H, Stadler B, Caruso F, Mulvaney P, Wrachtrup J and Hollenberg L C L 2009 arXiv:0911.4539v1

[9] Kurtsiefer C, Mayer S, Zarda P and Weinfurter H 2000 *Phys. Rev. Lett.* **85** 290

[10] Balasubramanian G *et al* 2009 *Nat. Mater.* **8** 383

[11] Neumann P, Mizouchi N, Rempp F, Hemmer P, Watanabe H, Yamasaki S, Jacques V, Gaebel T, Jelezko F and Wrachtrup J 2008 *Science* **320** 1326

[12] Harrison J, Sellars M J and Manson N B 2004 *J. Lumin.* **107** 245
Jelezko F and Wrachtrup J 2004 *J. Phys.: Condens. Matter* **16** 1089

[13] du Preez L 1965 *PhD Thesis* University of the Witwatersand

[14] Rogers L J, Armstrong S, Sellars M J and Manson N B 2008 *New J. Phys.* **10** 103024

[15] Reddy N R S, Manson N B and Krausz E R 1987 *J. Lumin.* **38** 46

[16] Batalov A, Jacques V, Kaiser F, Siyushev P, Neumann P, Rogers L J, McMurtrie R L, Manson N B, Jelezko F and Wrachtrup J 2009 *Phys. Rev. Lett.* **102** 195506

[17] Neumann P *et al* 2009 *New J. Phys.* **11** 013017

[18] Tamarat P H *et al* 2006 *New J. Phys.* **10** 045004

[19] Rogers L J *et al* 2009 *New J. Phys.* **11** 063007

[20] Fu K M C, Santori C, Barclay P E, Rogers L J, Manson N B and Beausoleil R G 2009 *Phys. Rev. Lett.* **103** 256404

[21] Loubser J H N and van Wyk J A 1978 *Rep. Prog. Phys.* **41** 1203

[22] He X-F, Manson N B and Fisk P T H 1993 *Phys. Rev.* B **47** 8816

[23] Lenef A and Rand S C 1996 *Phys. Rev.* B **53** 13441

[24] Manson N B, Harrison J P and Sellars M J 2006 *Phys. Rev.* B **74** 104304

[25] van Oort E and Glasbeek M 1990 *Chem. Phys. Lett.* **168** 529

[26] Felton S, Edmonds A M, Newton M E, Martineau P M, Fisher D, Twitchen D J and Baker J M 2009 *Phys. Rev.* B **79** 075203

[27] Goss J P, Jones R, Breyer S J, Briddon P R and Oberg S 1996 *Phys. Rev. Lett.* **77** 3041
Luszczek M, Laskowski R and Horodecki P 2004 *Physica* B **348** 292
Larsson J A and Delaney P 2008 *Phys. Rev.* B **77** 165201
Lin C, Wang Y, Chang H, Hayashi M and Lin S H 2008 *J. Chem. Phys.* **129** 124714
Gali A, Fyta M and Kaxiras E 2008 *Phys. Rev.* B **77** 155206

[28] Gali A, Janzen E, Deak P, Kresse G and Kaxiras E 2009 *Phys. Rev. Lett.* **103** 186404

[29] Hossain F M, Doherty M W, Wilson H and Hollenberg L C L 2008 *Phys. Rev. Lett.* **101** 226403

[30] Delaney P, Greer J C and Larsson J A 2010 *Nano Lett.* **10** 610

[31] Ma Y, Rohlfing M and Gali A 2010 *Phys. Rev.* B **81** 041204

[32] Cornwell J F 1997 *Group Theory in Physics: An Introduction* (London: Academic)

[33] Jackson J D 1998 *Classical Electrodynamics* (New York: Wiley)

[34] Maze J R 2010 *PhD Thesis* Harvard University, Cambridge, MA

[35] Delaney P, Larsson J A and Greer J C 2011 in preparation

[36] Drabenstedt A, Fleury L, Tietz C, Jelezko F, Kilin S, Nizovtzev A and Wrachtrup J 1999 *Phys. Rev.* B **60** 11503

[37] Tinkham M 2003 *Group Theory and Quantum Mechanics* (New York: Dover)

[38] Fischer G 1984 *Vibronic Coupling: The Interaction between the Electronic and Nuclear Motions* (London: Academic)

[39] Stoneham A M 1975 *Theory of Defects in Solids* (Oxford: Oxford University Press)